Mechanism and Position-Dependence of Inter-Unit Aerodynamic Coupling in Parallel Blower Systems

Paulo Cesar Correa Galeano[a,b,*], Yu-Jeng Lin[a] and Chen-yang Lan[a]

[a]Department of Mechanical Engineering, National Taiwan University of Science and Technology, Taipei City, 10607, Taiwan

[b]Department of Electromechanical Engineering, Taiwan-Paraguay Polytechnic University, Asunción, Paraguay

***Corresponding Author. Email:** pgaleano@uptp.edu.py

Abstract

When several blowers discharge into a shared manifold they operate against a common pressure rise and are coupled aerodynamically, yet the mechanism and position-dependence of this coupling have rarely been characterized experimentally. Unlike the inflow coupling of distributed propulsor arrays or the near-surge interaction of parallel compressors, the coupling in a blower manifold operating far from surge is transmitted pneumatically through the gas volume of the shared discharge manifold. This work characterizes it in an operating four-blower manifold from synchronized measurements of manifold pressure, blower flow and power, across different configurations. A multiple-input single-output regression identifies the steady-state coupling and reveals a non-monotonic dependence on position: adjacent blowers couple most weakly in the power domain, while a pressure-domain analysis recovers its true strength. A directional transient analysis confirms this mechanism: the target blower's flow responds sign-coherently to a neighbor's setpoint step, decreasing for an upward step and increasing for a downward one. Spectral and statistical analysis places the system in a quasi-static regime. The coupling is thus real, directional, and mechanistically identifiable, establishing pneumatic head-loading as the governing inter-unit interaction in shared-manifold blower systems.

Keywords: Aerodynamic Coupling; Parallel Blowers; Fan Array; Flow-Induced Pressure Fluctuations; Experimental Characterization; Disturbance Transmission Ratio.

1. Introduction

Parallel blowers discharging into a shared duct network are widespread in industrial aeration, mine ventilation, air-handling, and large process-air systems, where they are frequently operated not as isolated units but as parallel assemblies supplying a common discharge manifold (Czyżewicz et al. 2022). In such configurations, all simultaneously active machines discharge against a single shared system pressure rise that couples them aerodynamically, so that the collective behavior of the assembly, rather than that of any individual unit, governs its performance (Arya 2025). The mechanism and position-dependence of this inter-unit coupling, however, remain largely uncharacterized experimentally.

Such systems are also significant energy consumers, fans alone account for roughly a fifth of industrial motor-driven electricity use (Rao et al. 2021), which has driven extensive research on their efficient operation: variable-speed control (Shim et al. 2014), (Chatterjee et al. 2015), (Siddiqui et al. 2025), model-based and learning control (Shi et al. 2024), (Fulpagare et al. 2022, 2025), system-level reconfiguration (De Souza 2015), (Gunner et al. 2016), and fan-array optimization and data-driven performance modeling (Ostmann et al. 2022), (Conrad et al. 2023), (Ostmann et al. 2024), (Czyżewicz et al. 2022). Across these strands the machines are treated either in isolation or only in aggregate, and the inter-unit aerodynamic coupling is assumed known or neglected rather than resolved from measurement. Even the closest experimental study, a combined two-fan characteristic in a flexible duct (Dong and Jiang 2025), attributes no share of the interaction to individual machines or to position.

While the literature reviewed above treats fans as isolated units, or resolves them only in aggregate, the interaction between neighboring machines has itself received attention in the propulsion and turbomachinery communities. In distributed electric propulsion (DEP), arrays of ducted fans mounted along a wing are strongly coupled: the throttle setting of one fan alters the local inflow and loading of its neighbors, producing non-linear, position-dependent changes in thrust, lift, and efficiency. This propulsor cross-coupling has been characterized experimentally for wing-integrated arrays under varied throttle and placement (Perry et al. 2018; Jia et al. 2025; Weinstein et al. 2026). The related parallel-compressor literature, such as the work of Su et al. (Su et al. 2023), instead concerns high-speed instability and surge avoidance. Across these studies, the geometries and objectives differ from those of ventilation, and the characterizations are obtained

almost exclusively in wind tunnels, dedicated test rigs, or high-fidelity simulations. The mechanism also differs: propulsor arrays couple through an open external inflow field, one rotor's wake altering a neighbor's inlet condition; parallel compressors, through near-surge dynamics at high pressure ratio. The blowers considered here instead discharge into a shared duct, so the coupling is aerodynamic in origin but transmitted pneumatically rather than through blade-row inflow, a path whose mechanism and position-dependence remain uncharacterized.

Parallel blower systems have thus seen little full-scale experimental characterization: whereas the analogous interaction has been quantified for propulsor arrays and parallel compressors, the aerodynamic coupling transmitted pneumatically between blowers discharging into a shared industrial manifold has not been characterized. The present work identifies coupling directly from synchronized measurements on a full-scale blower system, resolving its mechanism, quasi-static head-loading through the shared manifold, and its non-monotonic dependence on position.

This work is organized around four questions. First, does a steady-state aerodynamic coupling exist between the blowers, and does its strength depend on position? Second, what is the mechanism of that coupling, and does its transient, directional response reveal it? Third, what manifold pressure fluctuations do parallel operations produce, and what dynamic regime do they represent? Fourth, and secondarily, what are the energetic implications? Sections 3–6 address these questions in turn, and Section 7 concludes.

2. Experimental System

2.1 Test System, Instrumentation, and Data Acquisition

The test system is an industrial aeration manifold comprising four high-speed turbo blowers discharging into a shared distribution header. The header feeds a biological aeration basin through diffusers submerged below the liquid surface, so the delivered air passes directly into the mixed liquor; the manifold differential pressure measured at the blower discharge therefore reflects the hydrostatic head of the diffuser submergence together with the distribution-piping losses. The blowers are arranged along the header in the order A–B–C–D, with Blower D at one extremity serving as the instrumented target, as shown in Figure 1.

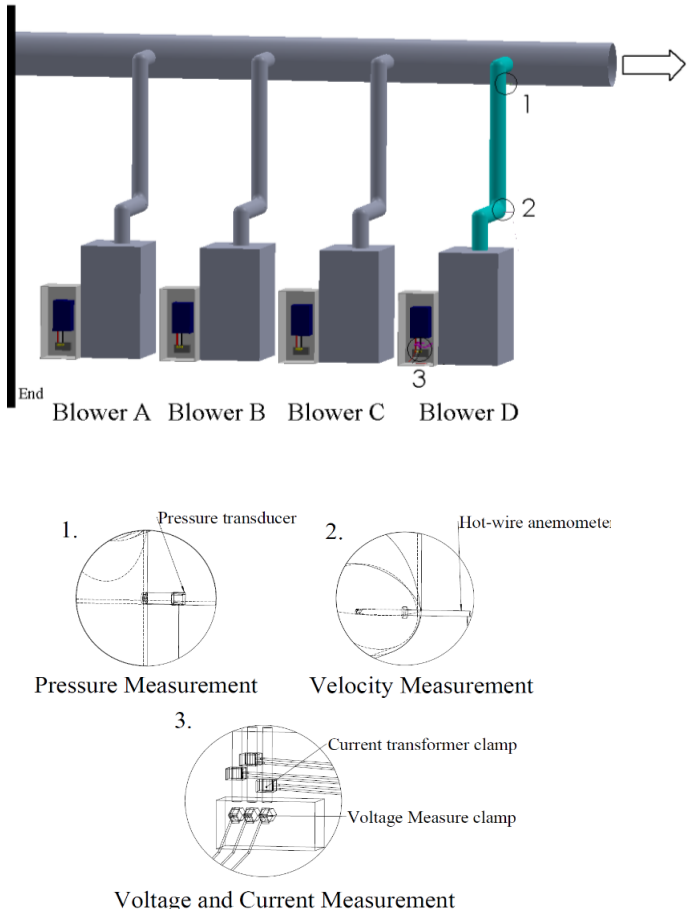


Figure 1. Test system overview and sensor setup diagram: (1) Outlet Pressure Measurement, (2) Outlet Velocity Measurement, (3) Voltage and Current Measurement.

Each blower is driven by an integrated variable-frequency drive, and its operating setpoint is commanded as a percentage of full speed; the experimental study used setpoints from 50% to 70%. The blower and manifold parameters are summarized in Table 1.

Parameter	Value
Blower model	Aerzen AT100-0.6S G5plus
Motor rating	80 kW
Speed range	9,000 – 29,000 RPM (VFD)
Discharge connection	DN200 (A_d= 0.03142 m²)

Table 1. Blower and manifold specifications.

By operating protocol, exactly three of the four blowers are active simultaneously. Two manifold configurations are studied. In the ACD configuration, blowers A, C, and D are active, and Blower B is idle; in the BCD configuration, blowers B, C, and D are active, and Blower A is idle. Blower D is the target blower throughout, and the other active blowers are referred to as neighbor blowers. Holding the operational state of blowers C and D constant isolates the impact of neighbor-blower position on Blower D's coupling behavior. Each blower is commanded at one of three VFD setpoints (50%, 60% and 70%) corresponding to shaft speeds of 14,500, 17,400, and 20,300 RPM and impeller tip speeds of 110.8, 133.0 and 155.2 m/s respectively.

Three quantities are recorded: the manifold differential pressure Δp, the volumetric flow rate of Blower D (Q_D), and the three-phase electrical power of Blower D (P_D), measured at locations (1), (2) and (3) of Figure 1 respectively; their acquisition settings are summarized in Online Resource 1. The differential pressure and Blower D flow are acquired continuously and recorded at 1 Hz, downsampled from a 1 kHz acquisition. The electrical power is measured at high frequency using National Instruments modules (NI-9244 voltage and NI-9227 current) sampling at 25,000 samples per second, from which the instantaneous three-phase power is computed. Owing to storage constraints, the high-frequency power is recorded in bursts of 19.5 seconds within each one-minute interval and is subsequently block-averaged to a 1 Hz series, time-aligned with the pressure and flow channels. All channels were acquired and logged in LabVIEW; full instrument accuracy specifications are listed in Online Resource 2.

The anemometer was placed at the duct centerline to measure air velocity. Since the blower inlet pressure is approximately equal to atmospheric pressure, the inlet pressure was set as 1 atm. Each measurement run lasted 20–30 minutes. The centerline placement of the FTM35 anemometer means the measured velocity exceeds the cross-sectional mean, so recovering the true volumetric flow would require a velocity-profile correction; that correction was not applied, and the resulting systematic bias is bounded here. For air ($\rho \approx 1.2\ \mathrm{kg/m^3}$, $\mu \approx 1.8 \times 10^{-5}\ \mathrm{Pa{\cdot}s}$) discharging through the DN200 duct ($d = 0.200$ m, $A_d = 0.03142\ \mathrm{m^2}$), the pipe Reynolds number $\mathrm{Re} = \rho V d/\mu$, with V the measured centerline velocity, is of order $3–5\times10^5$ across the 50–70% setpoints, so the discharge flow is fully turbulent. With 3 m of straight duct upstream of the probe (15 times the pipe diameter), the profile is taken as approximately fully developed. For fully developed turbulent pipe flow the mean-to-centerline velocity ratio follows the power-law profile $\bar{V}/V_c = 2n^2/[(n+1)(2n+1)]$, where $\bar{V}$ is the cross-sectional mean velocity, V_c the centerline velocity

and n the power-law exponent; taking n = 7, typical at Re $\approx 10^5$, gives a profile factor of 0.817 (Schlichting (Deceased) and Gersten 2017). Because the factor was not applied, flows are reported as $Q = V_c \cdot A_d$ directly from the centerline velocity and therefore overstate the true volumetric flow by 17–22%, depending on the profile exponent (n ≈ 7–9) over the measured Reynolds-number range.

This profile-factor bias is systematic and common to all flow channels: it scales every coupling coefficient α_j identically and therefore cancels exactly in the SPI (Section 3.1) and in every between-configuration comparison. It affects only the absolute magnitude of the coupling coefficients, not their ordering or their ratios, so the non-monotonic result of Section 3.2 and the SPI-based conclusions are invariant to it.

Two dimensionless groups characterize the range of measured operating conditions and recur in the coupling model of Section 3.3. Using the impeller tip speed $U = \omega R_{imp}$ (angular speed ω, impeller radius $R_{imp} \approx 0.073$ m), the flow coefficient is $\varphi = Q/(U \cdot A_d)$ and the head coefficient is $\psi = 2\Delta p/(\rho U^2)$. Because Q derives from the uncorrected centerline velocity (Section 2.1), φ carries the same 17–22% high bias, while ψ is not affected.

2.2 Experimental Protocol and Data Pre-Processing

The experimental sessions were conducted in two stages on an operating industrial facility, where experimental access was limited by production requirements. In the first, screening stage, each blower was perturbed individually across setpoints of 50, 55, 60 and 65% while the two remaining active blowers were held at their nominal 60% operating point, isolating each blower's own power-flow characteristic. This stage revealed that Blower D exhibited the weakest agreement between its power and its own flow, suggesting that its power was influenced by other active blowers.

The screening result motivated a second, focused stage, in which Blower D was instrumented as the target and held at 50, 60 or 70% while other active blowers were varied across 50, 60 and 70% for the two configurations (A-C-D and B-C-D). The A-C-D configuration was characterized in a full session of 15 operating points, of which 6 were repeated in a separate session to assess reproducibility. For B-C-D, a comparable single session could not be completed: data

from the first session were partially lost, yielding 7 usable operating points, and a separate session provided a further 6, which are pooled to form the 13-point B-C-D dataset. This second-stage dataset forms the basis of the coupling identification developed in the remainder of the paper. The experimental sessions are summarized in Table 2.

Session Day	Configuration	Setpoints (%)	Test points	Duration per point (min)
		Stage 1: screening		
1	**A**-C-D	50, 55, 60, 65	4	30
2	**B**-C-D	50, 55, 60, 65	4	30
	A-B-**C**	50, 55, 60, 65	4	30
3	A-B-**D**	50, 55, 60, 65	4	30
		Stage 2: focused		
4	**A-C-D**	50, 60, 70	15	20
5	**B-C-D**	50, 60, 70	7	20
6	**A-C-D**	50, 60, 70	6	20
	B-C-D	50, 60, 70	6	20

Table 2. Experimental sessions summary. Bold letters denote the varied blower(s); other active blowers were held at 60% (screening) or as noted in the text.

Figure 2 shows representative raw power, flow and manifold pressure series for Blower D for A-C-D configuration. In the power series, two forms of contamination are visible: setpoint-transition transients and isolated external-disturbance artefacts. Together with spurious zero values in the power series during inter-burst gaps and at acquisition discontinuities. The zeros are not physical, since Blower D is never de-energized during a run, and are flagged as missing and excluded from analysis, so that all subsequent averages, regressions, and spectral estimates use only valid samples. The per-second three-phase power is computed from the 25 kHz voltage and current samples within each burst.

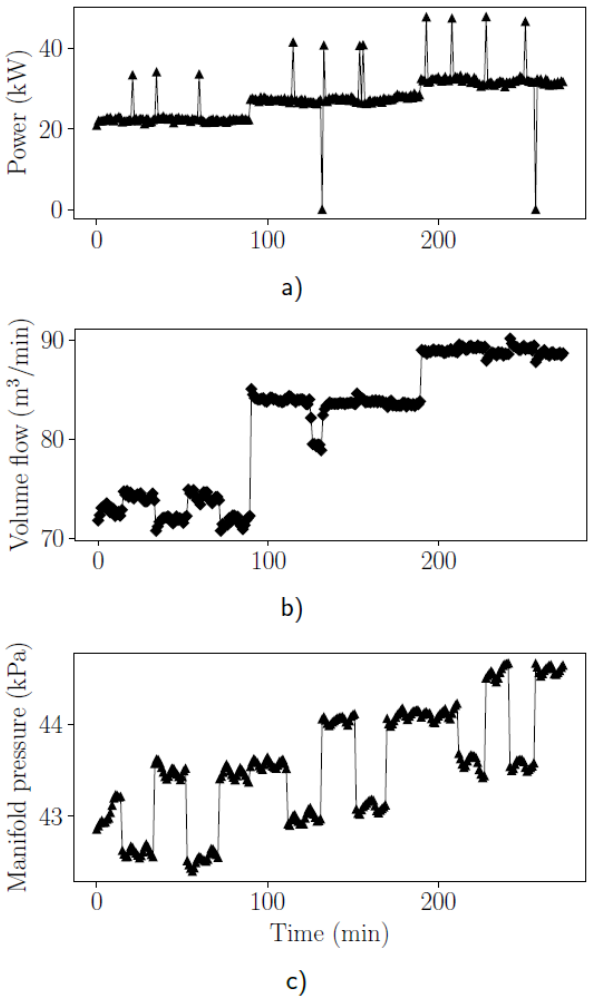


Figure 2. Raw time-series measurements of a) power, b) volume flow and c) manifold pressure from Session Day 4 configuration ACD, respectively.

The continuous record is segmented into operating points, each corresponding to a fixed combination of the three active blowers' setpoints, held to steady state for approximately 15–20 minutes each. Following each change in a neighbor blower setpoint, both the power and flow signals of Blower D exhibit a transient response lasting approximately 30 seconds to 2 minutes, during which the measurement does not represent a static operating point and must be excluded from the steady-state regression.

The two contamination types are removed in two stages. The first gates the time domain, applying a fixed exclusion window of 2 minutes following each recorded setpoint change event. This bound is conservative with respect to the longest observed transients and is consistent with the steady-state verification requirements of ISO 5801:2017, which specifies that measurements

in fan performance testing shall be taken only after the system has demonstrated stable operation, defined as less than 1% variation in the measured quantity over a specified observation window (International Organization for Standardization (ISO) 2017).

The second stage applies an interquartile-range fence ($k = 1.5$) independently within each operating point to remove residual isolated artefacts, excluding any point whose power value falls outside the fence. Across both configurations the two-stage filter retains more than 90% of the acquired samples, with exclusion dominated by the time-domain gate and the IQR stage contributing less than 1%.

All signal processing and statistical analysis were carried out in Python 3.14.3 using NumPy (Harris et al. 2020), SciPy (Virtanen et al. 2020), and statsmodels (Seabold and Perktold 2010). Power spectral densities and magnitude-squared coherence were computed with scipy.signal.welch and scipy.signal.coherence, using a Hann window, 512-s segments, 50% overlap, and linear detrending (applied to both the spectral density and the coherence). The coupling band spans periods of 30–512 s, the lower bound above the 2-s Nyquist period and the upper bound set by the segment length. Band integrals were calculated using scipy.integrate.trapezoid, and excess kurtosis with scipy.stats.kurtosis, considering the Fisher definition. Regression, Breusch–Pagan testing, and HC3 standard errors used statsmodels, as described in Section 3.1.

2.3 Measurement Uncertainty

The instrument accuracies are the manufacturer specifications; the full per-instrument budget is given in Online Resource 2. Propagating them shows that the dominant contribution to every power-based result is the current-transformer gain error, and that this systematic component largely cancels in the deviation ratios and configuration comparisons on which the conclusions rest.

All instruments were factory-calibrated against standards traceable to national metrology institutes, and the manufacturer accuracies were carried unchanged through the analysis. Three terms set the uncertainty scale: the current transformers (±3%), which dominate the power chain; the pressure transducer (±0.5% FS, ≈1 kPa); and the hot-wire anemometer (±2% of reading). The

NI acquisition modules (±0.17–0.41% of reading) are an order of magnitude smaller, and the NI-9244 samples the phase voltage directly, without an intervening potential transformer.

The error sources divide into systematic and random components, which propagate differently. The systematic components, namely the CT gain error, the pressure-transducer full-scale error, and the hot-wire calibration factor, are fixed biases of a given sensor over a session; because every power-based result is a ratio or difference of two values from the same chain (the SPI, the NDTR, and the ACD/BCD ratio), the CT gain error cancels to first order. The random components (quantization, electrical noise, turbulence-induced hot-wire scatter, and the block-averaging residual) are suppressed by averaging over the 20–30 min windows and the N = 13–15 operating-point means, so the raw ±3% figure overstates the uncertainty of the reported quantities.

For the derived quantities, the three-phase power adds the voltage and current terms in quadrature, and the SPI inherits the HC3 standard errors of Section 3.1 without further estimate; the remaining quantities propagate as follows. For the Normalized Disturbance Transmission Ratio (NDTR), $\eta = (\delta P_D/P_{pre})/(\Delta u/u_{nom})$, the setpoints are commanded digitally, so Δu and u_nom are treated as exact, and the expression is reduced to the two power terms. The Coupling Energy Index, CEI_m (Eq. (5.2)), i.e., the coherence-weighted integral of the pressure spectral density over the 1/512–1/30 Hz analysis band, scales as pressure squared, so the pressure-sensor term enters doubled and the Welch spectral estimator adds a variance set by the number of averaging segments K. The coherence weighting adds a further term: with few segments the estimated coherence γ_m^2 is biased upward (by approximately 1/K for incoherent signals), which sets a floor below which an estimated coherence cannot be distinguished from zero. The transient energy, $E_{trans,k} = \delta P_{D\,k} \cdot t_{settle}/60$, takes the settling-time uncertainty directly, together with the decay-profile uncertainty: the rectangular bound of the equation exceeds a triangular or exponential decay by approximately a factor of two, which is carried as the lower bound.

Combining the NI-9244 (±0.17%), NI-9227 (±0.37%), and current-transformer (±3%) terms in quadrature gives a relative standard uncertainty $u(P)/P = \sqrt{(0.17^2 + 0.37^2 + 3.0^2)}\% \approx 3.0\%$, dominated by the transformer; this component is systematic and cancels in the SPI and NDTR ratios, as the pressure-transducer gain error does in the ACD/BCD CEI ratio. The dominant uncertainty in the transient energy is instead the settling-time assumption, characterized in Section 6.2, which likewise cancels in the configuration ratio.

The cross-session reproducibility of the regression provides an in-situ check on the combined random error of the full acquisition-and-processing chain: α_D and α_C reproduced to within 0.02% and 0.6% across two independent sessions recorded on different days (Section 3.2), bounding the random error of the reported coefficients well below the ±3% raw instrument figure.

3. Steady-State Coupling Identification

3.1 MISO Regression Model and Sensitivity Placement Index

Because the three active blowers discharge into a common discharge manifold, each operates against the same instantaneous manifold pressure. Blower D's power is therefore a function not only of its own flow but of the flow contributed by every active blower. This dependence is represented linearly as a multiple-input single-output (MISO) model:

$$P_D = \beta_0 + \sum_{i \in \mathcal{A}} \alpha_i \cdot Q_i + \varepsilon \qquad (3.1)$$

where P_D is the operating-point-mean Blower D electrical power (kW), $\mathcal{A}$ is the set of blowers active in the configuration under test (three blowers, always including Blower D), Q_i. is the operating-point-mean volumetric flow of active blower i (m³/s), α_i. is the coupling coefficient of blower i: the marginal Blower D power per unit flow of that blower (kW·s/m³), with, α_D the self-coupling term β_0 is the intercept (kW), and ε is the zero-mean residual. Since only Blower D was instrumented for flow in the second-stage sessions; the neighbor-blower flows, Q_i for $i \neq D$ were therefore not measured concurrently but obtained from each blower's individually characterized power–flow relationship from the screening stage, interpolated linearly over the commanded setpoint.

The self-coupling coefficient α_D captures Blower D's own power–flow relationship; the cross-coupling coefficients α_i for $i \neq D$ quantify how much each of the other active blowers' flow contributes to Blower D's power through the shared manifold. A coefficient near zero would indicate aerodynamic independence; a positive coefficient indicates that increasing that blower's flow raises Blower D's power, the signature of head-loading coupling. Coefficients were estimated by ordinary least squares. Residual diagnostics indicated non-constant error variance across the range of measured operating conditions, confirmed by a Breusch-Pagan test. Inference therefore

used heteroscedasticity-consistent (HC3) standard errors, which give reliable finite-sample coverage for the small sample sizes (N = 13–15 operating points) encountered here. Confidence intervals on each coefficient follow from the HC3 standard errors and the t-distribution, and are reported per coefficient in Table 3. Estimation, diagnostics, and HC3 covariances used statsmodels (Seabold and Perktold 2010) and the setpoint interpolation SciPy (Virtanen et al. 2020).

To compare coupling strength across blowers on a common dimensionless scale, each cross-coupling coefficient is normalized to the self-coupling coefficient, defining the Sensitivity Placement Index (SPI):

$$SPI_j = \left(\frac{\alpha_j}{\alpha_D}\right) \times 100\% \quad (3.2)$$

The SPI expresses the influence of any active Blower j $\in \mathcal{A}$ on Blower D's power as a percentage of Blower D's influence on its own power. By construction $SPI_D. = 100$. A larger SPI indicates stronger coupling.

3.2 Identified Coefficients and Results

The identified flow-based power models for the two configurations are summarized in Table 3, which reports each coefficient together with its HC3 standard error, 95% confidence interval, and p-value. Every cross-coupling term is retained at the 5% level, and the intercepts and self-coupling terms are estimated with tight intervals in both configurations.

Config.	Term	α (kW·s/m³)	SE	95% CI	p-value
A-C-D	β_0	-24.253	0.994	[-26.21, -22.29]	<0.001
	α_D	0.5690	0.0081	[0.553, 0.585]	<0.001
	α_C	0.0166	0.0052	[0.006, 0.027]	0.0016
	α_A	0.0439	0.0075	[0.029, 0.059]	<0.001
B-C-D	β_0	-24.878	1.054	[-26.95, -22.80]	<0.001
	α_D	0.5689	0.0080	[0.553, 0.585]	<0.001
	α_C	0.0167	0.0052	[0.007, 0.027]	0.0015
	α_B	0.0518	0.0087	[0.035, 0.069]	<0.001

Table 3. Identified MISO regression parameters for both configurations. Standard errors and 95% confidence intervals are heteroscedasticity-consistent (HC3).

Normalizing the identified cross-coupling coefficients from both configurations against Blower D's self-coupling term gives the power-domain SPI, listed with its pressure-domain

counterpart in Section 5.2. Ordering the blowers by SPI shows that coupling strength is not monotonic in physical distance: the near blower A is the strongest contributor (9.10%), the far blower E ranks second (7.71%), and the adjacent blower C is the weakest (2.92%).

Both configurations use blowers D and C, providing an internal validation of the regression. Their coefficients reproduce across the two independent sessions, recorded on different days, to within tight tolerances: the relative differences are 0.02% for α_D and 0.6% for α_C. These confirm that the regression captures a stable physical relationship rather than session-specific artefacts.

The central result of the regression is that the coupling does not decrease monotonically with distance from the target. The adjacent Blower C produces the weakest power coupling (2.92%), while the more distant blowers A (7.71%) and B (9.10%) produce stronger coupling, with $\alpha_C < \alpha_A < \alpha_B$. The coupling of Blower C being the weakest is more robust than the ordering between the respective couplings of blowers A and B, since the HC3 confidence interval on the difference, $CI(\alpha_B - \alpha_A) = [-0.017, +0.033]$, overlaps zero.

One interpretation is that a small steady-state coefficient does not necessarily indicate a weak response to the shared manifold. Because all three blowers discharge into a common header, a step at Blower C reaches Blower D through the resulting rise in manifold pressure, but that rise acts on Blower D's power through two terms of opposite sign: at Blower D's existing flow the higher head increases the work it must do, while the same rise pushes Blower D back along its own characteristic and reduces its flow, which decreases that work. Where the two contributions are comparable in magnitude, the net steady-state coupling would be small even though neither term is individually negligible, so the small coefficient would reflect a cancellation between two active mechanisms rather than the absence of interaction. Because the two terms are not established on the same timescale, a steady-state coefficient would also understate the transient response to a step. Section 3.3 examines this interpretation through a linearized model of the system.

3.3 Linearized Manifold Model and the Cancellation Condition

Section 3.2 identified the two opposing terms qualitatively and advanced their near-cancellation as an interpretation of the non-monotonic ordering but did not derive the condition under which they balance. A linearized model of the shared manifold makes both terms explicit, fixes the cancellation condition in terms of the measurable characteristic slope, and recasts that

condition in the dimensionless slope of the blower characteristic to state when it should be expected to arise.

The model begins with three active blowers discharging into a single header at a common differential pressure Δp. Linearizing each blower's pressure–flow characteristic about the operating point gives, for any blower i:

$$\delta(\Delta p) = a_i \cdot \delta Q_i + b_i \cdot \delta u_i \quad (3.3)$$

with $a_i = \partial \Delta p / \partial Q_i < 0$ the local slope of the falling Δp–Q curve and $b_i = \partial \Delta p / \partial u_i > 0$ the setpoint gain with respect to the commanded VFD setpoint u_i(% of full speed), where $b_i \cdot \delta u_i = 0$ for every blower except the one being stepped. The header is closed by the system resistance curve and continuity, respectively:

$$\delta(\Delta p) = r \cdot \delta Q_{tot}, \; r > 0 \quad (3.4)$$

where $\delta Q_{tot} = \Sigma_i \, \delta Q_i$. Consider now a step applied to Blower C alone ($\delta u_C > 0$, $\delta u_D = \delta u_A = 0$). Each unstepped blower responds only through the shared pressure, $\delta Q_i = \delta(\Delta p)/a_i$. The stepped blower itself carries the source term, $\delta Q_C = [\delta \Delta p - b_C \cdot \delta u_C]/a_C$. Substituting both relations into the resistance relation (Eq. (3.4)) with continuity and solving for the manifold pressure response gives:

$$\delta(\Delta p) = [\, -(r/a_C) \cdot b_C \cdot \delta u_C \,] \,/\, [\, 1 - r \cdot (1/a_C + 1/a_D + 1/a_A) \,] \quad (3.5)$$

which is positive because every $a_i < 0$: an upward step at Blower C raises the shared manifold pressure by an amount fixed entirely by the measurable characteristic slopes.

Blower D feels that pressure rise through two competing terms in its power balance. With Blower D's power written as $P_D = \Delta p \cdot Q_D / \eta_f$, where η_f is Blower D's overall efficiency, assumed constant over the small perturbation, the first-order power perturbation is:

$$\delta P_D = (1/\eta_f)[\, Q_D \cdot \delta(\Delta p) + \Delta p \cdot \delta Q_D \,] = (\delta(\Delta p)/\eta_f)[\, Q_D + \Delta p / a_D \,] \quad (3.6)$$

The bracket exposes both terms directly. The first term, $Q_D > 0$, is head-loading: the manifold pressure rise loads Blower D at its current flow. The second term, $\Delta p / a_D < 0$ (since $a_D < 0$), is flow recession: the same pressure rise pushes Blower D back down its own characteristic, reducing its flow. The net steady-state power coupling is small when $Q_D \approx$

$|\Delta p/a_D|$, i.e. when the operating point sits where the two terms are comparable, precisely the near-cancellation proposed in Section 3.2 to explain the small power SPI of the adjacent Blower C, here obtained as a result of the model rather than assumed. The more distant blowers A and B reach Blower D almost entirely through the pressure term, with negligible direct-flow cancellation, and therefore impose the larger net coupling.

The two terms do not act at the same instant. The pressure perturbation propagates acoustically and is therefore effectively instantaneous relative to the flow redistribution, which is rate-limited by duct inertance. Immediately after the step $\delta Q_D \approx 0$ and only the head-loading term acts; at steady state both terms are present:

$$\text{Transient:} \quad \delta P_D \approx Q_D \cdot \delta(\Delta p)/\eta_f \quad (3.7)$$

$$\text{Steady state:} \quad \delta P_D = (Q_D + \Delta p/a_D) \cdot \delta(\Delta p)/\eta_f \quad (3.8)$$

As written, the cancellation condition is dimensional and specific to this installation. Expressing the characteristic slope in the flow and head coefficients $\varphi = Q/(U \cdot A_d)$ and $\psi = 2\Delta p/(\rho U^2)$ (Section 2.1, tip speed $U = \omega R_{imp}$), the slope becomes $a_D = (\rho U/2A_d) \cdot (d\psi/d\varphi)$.The cancellation condition $Q_D \approx |\Delta p/a_D|$ then reduces to a condition on the local slope of the dimensionless characteristic:

$$\varphi \cdot (d\psi/d\varphi) \approx -\psi \quad (3.9)$$

Because Eq. (3.9) is written entirely in dimensionless quantities, the near-cancellation of the adjacent-blower power coupling is not tied to the dimensions of this installation and is expected to extend to geometrically similar machines operating where the characteristic slope satisfies it, subject to verification on other installations. Verifying Eq. (3.9) against the present data, by extracting a_D from Blower D's own Δp–Q curve and comparing $Q_D$with $|\Delta p/a_D|$, is a direct test of the interpretation advanced in Section 3.2 and is left to future work.

One limitation follows from the lumping. Because all blowers share a single pressure node in this model, it does not by itself reproduce the position dependence of the coupling (Blower C versus B versus A). The position-dependent coupling strengths enter through the inter-blower branch impedances of the physical header, which the lumped model absorbs into the effective slopes a_i and resistance r; resolving them spatially is not attempted here, and the model is used

only to establish the form of the cancellation condition rather than to predict the position dependence.

4. Directional Sensitivity Analysis

The raw power and flow signals recorded immediately after each scheduled setpoint step carry information that steady-state averaging discards: the direction of coupling, that is, whether upward and downward steps couple differently; the relative timing of the power and flow responses; and the dependence of the coupling on a third blower's operating state.

4.1 Method: Sessions, NDTR Definition, and Peak Extraction

Four experimental sessions contributed data to this section as listed in Online Resource 3. Only events in which a single blower steps while all others remain constant are used in the primary directional means, so that the response can be attributed unambiguously to one blower. Events in which Blower D steps concurrently with another blower are excluded. The post-step transients excluded from the steady-state regression are used here, since the peak search requires their time structure.

The Normalized Disturbance Transmission Ratio (NDTR) quantifies the fractional signal deviation at Blower D per unit fractional setpoint change at any other blower. A single ratio is defined for either magnitude, with θ denoting the assessed quantity, Blower D's power P or its flow Q,

$$\eta_k^{\theta} = \frac{\frac{d\theta_{D,k}}{\theta_{pre,k}}}{\frac{|du_{j,k}|}{u_{nom}}} \qquad (4.1)$$

where θ is the assessed quantity at Blower D, either its power (kW) or its flow (m³/s); $d\theta_{D,k}$ is the peak deviation of that quantity within the corresponding search window, taken as the maximum positive excursion for power and the minimum signed excursion for flow; $\theta_{pre,k}$ is the pre-step plateau value of the same quantity (mean of final 3 min before step); $|du_{j,k}|$is the absolute setpoint step magnitude of blower j (%); and u_{nom} = 60% is the normalization reference setpoint.

These formulations are structurally equivalent to the normalized open-loop step-response gain of Ljung (Ljung 1999) and to the Bristol Relative Gain Array interaction measure (Bristol 1966), adapted here to a single instrumented output (Blower D) with multiple disturbance inputs (the other blowers). The power NDTR uses the absolute peak because coupling events always raise Blower D's power; the flow NDTR retains its sign because the direction of the flow excursion is itself diagnostic.

When a blower changes its setpoint, the perturbation reaches Blower D first as a pressure wave and only later as a flow redistribution. The pressure wave travels at the speed of sound (around 343 m/s) and crosses the approximately 8 m manifold in about 0.02 s, instantaneous on the 1 Hz sampling grid, so Blower D's power responds within the first sampling interval, whereas the bulk flow response is governed by the duct inertance L/A and evolves according to the unsteady momentum balance, $\frac{dQ}{dt} = \left(\frac{1}{L/A}\right) \cdot (dP_{fan} - dP_{manifold})$. Because L/A is larger for blowers further from the manifold outlet (L and A being the length and cross-sectional area of the duct path from the blower to the manifold, and $\rho L/A$ the acoustic inertance, with ρ the air density), this equation predicts that the power signal peaks earlier than the flow signal, with a lag that grows with the inertance of the affected path. For each single-blower upward step the times of maximum power deviation and minimum flow deviation were located independently within a wide 5-minute window; the power-before-flow lag was significant (one-sample t-test, $p < 0.05$), and the 95th-percentile peak times plus a 0.5-minute safety margin set the adopted window widths of $t_{win,P} =$ 2.0 min for the fast power peak and $t_{win,Q} = 3.0$ min for the slow flow trough.

Unlike the power NDTR, which uses the absolute peak (always positive for coupling events), the flow NDTR retains the sign of $dQ_{D,k}$. This sign carries direct physical meaning: $\eta^Q <$ 0 for upward steps ($\Delta u > 0$) blower D's flow decreases when any blower steps up. The higher manifold pressure pushes Blower D toward lower volumetric output along its Δp–Q characteristic. $\eta^Q > 0$ for downward steps ($\Delta u < 0$) blower D's flow increases when any blower steps down. The lower manifold pressure allows Blower D to deliver more flow.

This sign pattern, negative flow NDTR for upward steps, positive for downward, is the aerodynamic signature of manifold pressure coupling. It is opposite to what a direct flow-addition (non-coupled) mechanism would produce, where an increase in a neighbor blower's flow would,

if anything, raise the total and not suppress Blower D's individual delivery. The observed sign therefore distinguishes genuine shared-pressure coupling from mere flow superposition.

For each step-change event k, two peak deviations are extracted from Blower D's raw signals relative to the pre-step plateau. The power deviation $\delta P_{D,k}$ is the maximum positive excursion within the power search window:

$$\delta P_{D,k} = max\{ P_D(t) - P_{pre,k} \mid t\ in\ [t_{step}, t_{step} + t_{win,P}\ ]\ \} \quad (4.2)$$

The pre-step plateau, $P_{pre,k}$ is the mean power of the final 3 minutes of the clean plateau preceding step k, and t_{step} is the time at which the setpoint step is commanded. The signed flow deviation $\delta Q_{D,k}$ is the corresponding minimum (most negative) excursion within the flow search window, where $Q_{pre,k}$ is the pre-step flow plateau defined in the same way as $P_{pre,k}$:

$$\delta Q_{D,k} = min\{ Q_D(t) - Q_{pre,k} \mid t\ in\ [t_{step}, t_{step} + t_{win,Q}]\ \} \quad (4.3)$$

Each candidate power response was validated against the concurrent flow signal. A power excursion was accepted as a genuine coupling response only when a corresponding flow deviation occurred at the same time; isolated power excursions with no concurrent flow response were identified as electrical artifacts and excluded from the analysis. This criterion was applied uniformly to all events.

The directional mean NDTR values are defined for each magnitude θ, with the subscript ± denoting the sign of the setpoint step:

$$S\pm^{\theta} = mean(\ \eta_k^{\theta} \mid sgn(du) = \pm). \quad (4.4)$$

The principal hypothesis tested is the directional sign reversal of Blower D's flow response: the flow NDTR is negative for upward steps ($\Delta u > 0$) and positive for downward steps ($\Delta u < 0$). A secondary hypothesis holds that the power channel shows the same directional asymmetry: $H1$: $S+^{P} > |S-^{P}|$. The dispersion of each directional mean across the tested setpoint levels reported as the standard deviation of η, or as the range where only a small number of events is available. The coefficient of variation is not used because the NDTR values are small and, in several cases, change sign across the tested setpoint levels, the coefficient of variation is undefined or uninformative as the mean approaches zero. The standard deviation is instead reported as a descriptive dispersion measure only, and the consistency of the flow response is characterized by the reliability of its sign across events, assessed by a sign test and by a Fisher exact test of step direction against response sign, rather than by its relative variance.

4.2 Flow and Power NDTR Results

The signed flow NDTR is the central result of this section. Across every valid upward step, the flow NDTR is negative: a neighbor blower's upward step reduces Blower D's flow. Across downward steps it is predominantly positive: a neighbor blower's downward step increases Blower D's flow. Eleven of eleven valid upward events show a negative flow NDTR (sign test, $p = 0.001$), with one further upward event excluded because of a pre-step baseline drift. The downward direction is positive in six of eight events, which is not individually statistically significant. This directional sign reversal is the signature of manifold head-loading coupling, and it is the finding on which this section rests.

The sign reversal is mechanistically diagnostic rather than incidental. A direct flow-addition mechanism would not suppress Blower D's delivery when a neighbor blower steps up; only a shared-pressure pathway produces suppression on upward steps and relief on downward ones. The consistency of the effect across all eleven valid upward events, extending to both configurations and the full range of the tested setpoint levels, establishes the coupling independently of the power channel.

The flow response reveals a clear directional structure that the power channel does not. Fig. 3a shows the flow NDTR for every step event, separated by direction. Upward steps of a neighbor blower consistently reduce Blower D's flow (negative flow NDTR), and downward steps increase it (positive flow NDTR). This sign reversal is the defining signature of head-loading coupling through the shared manifold pressure: when a neighbor blower raises its output, the manifold pressure rises and pushes Blower D back along its own characteristic, reducing its flow; the reverse occurs when a neighbor blower reduces its output. A direct flow-addition mechanism would produce the opposite sign pattern. The signature is highly reliable, all eleven valid upward events are negative, whereas the corresponding power response shows no consistent relationship between step direction and sign (Fig. 3, Table 4), confirming that the directional coupling is carried by flow redistribution rather than by a directional change in Blower D's power.

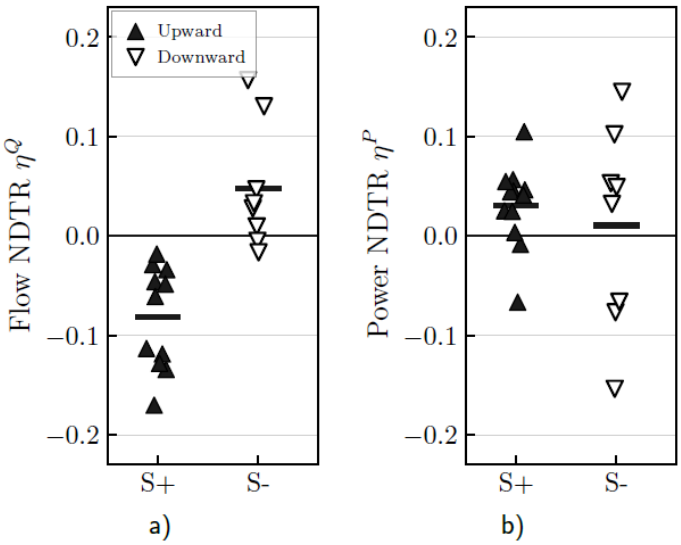


Figure 3. a) Flow and b) power NDTR by step direction.

Table 4 collects the directional mean power and flow NDTR, with event counts and dispersion, for every reliable event group. In the power channel the adjacent Blower C in ACD is the best-covered case: three upward events ($\Delta u_C = +20$) spanning low, mid, and high operating levels yield $S{+}_C^P = +0.069 \pm 0.032$, so a 1% rise in Blower C's setpoint changes Blower D's power by less than a tenth of a percent. The downward direction gives $S{-}_C^P = +0.031 \pm 0.161$, a mean smaller than its own dispersion and therefore directionally unresolved. Both directional power means are small relative to their dispersion, so the power channel does not resolve the asymmetry $S{+}^P \gg |S{-}^P|$ of hypothesis H1. The head-loading mechanism is established instead by the flow channel, where the same Blower C events give a mean flow NDTR of -0.090 ± 0.062 on upward steps and $+0.071 \pm 0.076$ on downward steps.

Both blowers give comparably small power responses: Blower A at header position 3 gives $S{+}_A^P = +0.008 \pm 0.054$ (pooled over the two ACD sessions after a session-consistency check) and Blower B at position 2 gives $S{+}_B^P = +0.032 \pm 0.012$. Blower A's power mean is smaller than its own dispersion and, like the other power NDTR, should be read as directionally uninformative rather than precisely resolved; its longer flow path also carries the larger inertance.

Blower	Config	n	η_P (mean ± SD)	η_Q (mean ± SD)
S+ (upward step)				
C	ACD	3	+0.069 ± 0.032	−0.090 ± 0.062
C	BCD	2	+0.018 ± 0.037	−0.045 ± 0.023
B	BCD	3	+0.032 ± 0.012	−0.088 ± 0.047
A	ACD	4	+0.008 ± 0.054	−0.091 ± 0.070
S− (downward step)				
C	ACD	3	+0.031 ± 0.161	+0.071 ± 0.076
C	BCD	2	−0.012 ± 0.092	+0.079 ± 0.072
B	BCD	1	+0.032	−0.005
A	ACD	2	−0.008 ± 0.082	+0.008 ± 0.035

Table 4. Directional NDTR by step direction, blower, and configuration.

Flow and power NDTR both have small magnitude; therefore the coupling is not characterized by the size of either response but by whether the step direction determines the sign of the response. Step direction is a statistically significant predictor of the sign of the flow response (Fisher exact test, $p = 0.001$), but not of the sign of the power response ($p = 0.35$). The directional coupling is therefore expressed as a sign-coherent flow response, consistent with manifold head-loading: the step alters the manifold pressure, and that pressure change redistributes flow among the blowers discharging into the common header, while the power response carries no comparable directional signature. The small transient power coupling is consistent with the small steady-state power SPI reported in Section 3.2, where the adjacent Blower C contributes only 2.92% of Blower D's self-coupling term, so the transient and steady-state analyses agree. The power NDTR is uniformly small across all blowers and configurations, with no blower producing a dominant power response; the power channel therefore supports no cross-configuration ordering, and the steady-state regression of Section 3.2 remains the reference for relative power coupling strength.

4.3 Agreement Between Transient and Steady-State Coupling

The NDTR and the MISO regression measure related but distinct quantities: the regression coefficient αj is a steady-state gain (Blower D power per unit change in blower j flow, once settled), whereas $S{+}_j^P$ is a transient gain (peak fractional power excursion per unit fractional setpoint step). The two therefore differ in timescale (settled plateaus versus a transient peak within about 2 min), in mechanism (steady-state flow redistribution versus head perturbation during the transient), in

input variable (blower flow Q_j versus setpoint step Δu_j), and in directionality (a single symmetric coefficient versus separate S+ and S− means).

For Blower C the two analyses agree rather than conflict. Blower C has the weakest steady-state power SPI (2.92%) because its flow-recession and head-loading terms partially cancel once settled, and its transient power excursion is likewise small ($S+^{P} = +0.069 \pm 0.032$), so the cancellation that suppresses the steady-state term is not offset by a large transient one. The small transient power coupling is consistent with the small steady-state power SPI of Section 3.2, so the transient and steady-state analyses agree. The physical result is carried by the flow channel instead. Upward steps suppress Blower D's flow (-0.090 ± 0.062 for Blower C in ACD) and downward steps relieve it ($+0.071 \pm 0.076$), a sign reversal that only a shared-pressure pathway can produce, which identifies the mechanism as manifold head-loading. Recomputed over a grid of power, flow, and settling windows, $S+_{C}^{P}$ kept the sign of the flow NDTR unchanged in every valid event, so the directional result is not an artefact of window choice.

Three limitations qualify the directional results. First, as noted in Section 4.2, the downward-step flow response is not individually statistically significant; only the upward-step sign signature ($p = 0.001$) and the overall association between step direction and the sign of the flow response (Fisher exact test, $p = 0.001$) are significant. Second, the step magnitudes were asymmetric (+20% against −10%) to reflect the system's operating range; the NDTR normalization of Eq. (4.1) accounts for magnitude, but non-linearity between ±10% and ±20% cannot be excluded. Third, the 25 kHz power signal was burst-sampled in 19.5 s windows once per minute, so events whose peak fell in an inter-burst gap give a lower-bound $\delta P_{D,k}$; extraction was therefore restricted to events with burst coverage containing the peak.

5. Manifold Pressure Fluctuation Quantification

5.1 Signal Decomposition and Dynamic Regime

The manifold differential pressure is analyzed per operating point, each operating point being a fixed combination of the three active blowers' setpoints. Within operating point m the pressure signal is decomposed into a steady baseline and a zero-mean fluctuation:

$$\Delta p(t) = \overline{\Delta p_m} + \Delta p_m'(t) \quad t \text{ in operating point } m \quad (5.1)$$

where $\overline{\Delta p_m}$ is the operating-point-mean baseline pressure (kPa), from the settled second half of the operating point and $\Delta p_m'(t)$ is the zero-mean within-operating-point fluctuation (kPa), by construction $\langle \Delta p_m' \rangle = 0$.

An operating point is admitted to the spectral analysis only if it is genuinely settled, quantified by the acceptance criterion that the absolute mean of the de-trended fluctuation, relative to its standard deviation, is small, lesser than 0.10.

Two operating points from ACD session 4 and BCD session 5 fail this criterion because they contain the tail of a large preceding transient; they are excluded from the spectral analysis but retained for the steady-state regression, where the settled-half mean is still valid. The residual measurement noise floor, estimated from the quietest settled operating points, is $\sigma_{noise} = 0.052$ kPa and is used as the reference scale throughout this section.

Before the pressure fluctuations can be interpreted as coupling signatures, surge or rotating stall must be excluded. Figure 4a shows the fluctuation at an operating point common to both configurations (Blower A-B/C/D = 60/60/50); as Figure 4b shows, the fluctuation is platykurtic at every admitted operating point, so the point displayed is representative.

Liśkiewicz et al. (Liśkiewicz et al. 2014) established that excess kurtosis κ is a sensitive surge precursor in centrifugal blowers: heavy tails and intermittent spikes drive κ strongly positive as a machine approaches instability, whereas quasi-static operation yields a flat-topped, sub-Gaussian distribution with $\kappa < 0$. Here the excess kurtosis of the within-operating-point fluctuation is negative at every admitted operating point across all sessions, so the fluctuations are platykurtic, bounded, and free of the heavy tails and large excursions that accompany surge or rotating stall; none of the 32 admitted operating points shows incipient instability.

Consistent with this, the classification is corroborated by the Greitzer B-parameter (Greitzer 1976), the dimensionless group that governs whether a compression system responds to a perturbation quasi-statically or dynamically. A second check concerns acoustic rather than surge behavior: the Helmholtz resonance frequency, the natural frequency at which a plenum gas oscillates against the inertance of the discharge duct. Both parameters depend on the same plenum volume, which is therefore identified once here and used for both checks.

The relevant volume is the enclosed gas volume between the blower discharge and the submerged diffusers. The far larger aeration basin does not contribute to the pneumatic compliance: the air passes directly into the mixed liquor, so the basin acts as an open sink rather than a Greitzer plenum. As no discrete plenum vessel exists, the volume is estimated from the manifold and discharge-duct geometry and is therefore uncertain.

Because the Greitzer parameter scales with the square root of the plenum volume, the quasi-static classification is insensitive to this estimate: with the measured values of $B \approx 0.23 - 0.32$, the plenum volume would have to be underestimated by at least a factor of about 2.5 for B to reach the surge-onset threshold ($B \approx 0.5$), and by at least roughly a factor of five to reach the upper bound of the surge band. Evaluated from the Greitzer parameter $B = (U/2a) \cdot \sqrt{\left(V_p/(A_d \cdot L_d)\right)}$ (Greitzer 1976), where $a \approx 343$ m/s is the speed of sound, V_p the plenum volume and L_d the effective discharge-duct length, using the duct geometry and the estimated plenum volume (A_d = 0.03142 m² for the DN200 discharge, $V_p \approx 0.5$ m³, $L_d \approx 8$ m) and the impeller tip speed at each setpoint, $B = 0.228, 0.273$ and 0.319 at the 50%, 60% and 70% setpoints respectively, far below the critical threshold of approximately 0.5–0.7, confirming quasi-static operation, as shown in Figure 4c.

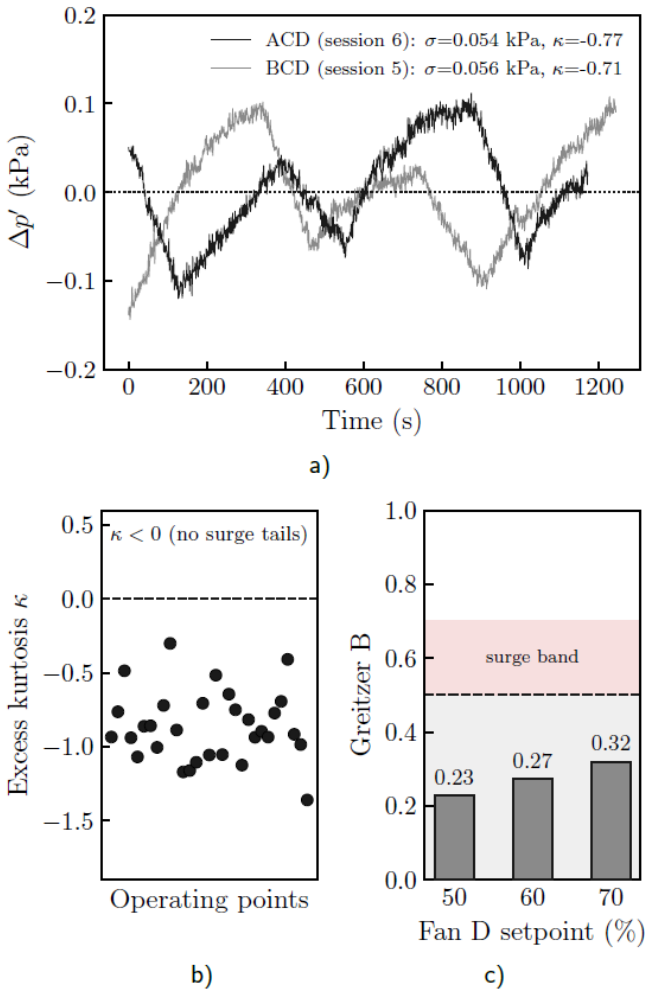


Figure 4. Dynamic regime of the manifold. (a) Manifold pressure fluctuation within a steady operating point (Blower A-B/C/D = 60/60/50). (b) Excess kurtosis of the pressure fluctuation at all admitted operating points. (c) Greitzer stability parameter B at each Blower D setpoint, computed from the system geometry and operating conditions.

The acoustic check confirms that the observed coupling-band oscillations are not a resonance of the plenum-duct system. Evaluated from the same geometry, the Helmholtz resonance frequency of the manifold, $f_H = (a/2\pi) \cdot \sqrt{\left(A_d/\left(V_p \cdot L_d\right)\right)}$, is $f_H \approx 4.8$ Hz (period, $T_H \approx 0.2$ s), which lies about three orders of magnitude away from the coupling band of interest, [30, 512] s. This separation is likewise insensitive to the plenum estimate: since the Helmholtz frequency scales with the inverse square root of the plenum volume, the estimated volume would have to be larger by roughly four orders of magnitude before the resonance descended into the coupling band. The slow coupling-band oscillations observed in the pressure signal are therefore

not Helmholtz resonance; they reflect the quasi-static redistribution of flow and pressure among the blowers in response to setpoint changes and control action.

The distribution shape thus establishes quasi-static operation independently of geometry, and both geometry-based checks agree with it, confirming the physical premise of the head-loading interpretation of Section 4.

5.2 Pressure-Domain Regression and Configuration Comparison

The manifold pressure is a shared variable to which every active blower contributes directly, the coupling is visible in the measured magnitudes before any model is fitted, as shown in Figure 5). Raising either active neighbor blower's setpoint from 50% to 70% increases Blower D's manifold pressure by approximately 1 kPa at every Blower D setpoint, far exceeding the within-operating-point fluctuation (approx. 0.06 kPa), so the coupling is resolved without any spectral or statistical processing. Both blowers A and C in the ACD produce this shift. Blower B in the BCD configuration, produces the same coupling, a shift of 0.97–1.04 kPa for a 50–70% step; its per-level dependence is not shown separately, as the partial, multi-session BCD dataset does not support a clean single-session curve. The figure establishes the coupling and its approximate magnitude; the regression that follows converts these shifts into per-blower coefficients on a common scale, comparable directly with the power-domain SPI of Section 3.

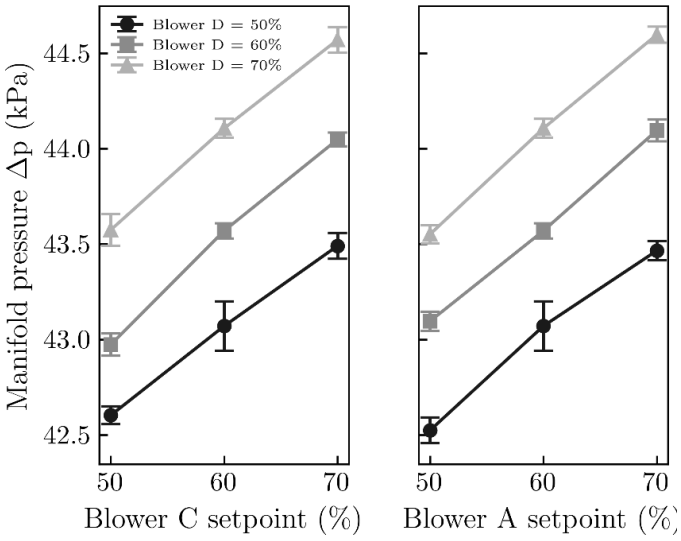


Figure 5. Inter-unit coupling in the pressure magnitude. Operating-point-mean manifold pressure at Blower D versus each active neighbor blower's setpoint, at three Blower D setpoints, in the ACD configuration: (a) varying Blower C (Blower A held at 60%); (b) varying Blower A (Blower C held at 60%).

The same MISO regression methodology applied to power in Section 3.1 is used to quantify these shifts. Equation (3.1) is now applied to the operating-point-mean manifold pressure, regressing Δp. on the active blowers' flows, with the pressure regression coefficients denoted Γ in place of the power-domain α terms. The pressure-domain Sensitivity Placement Index is defined exactly as in Eq. (3.2), with each cross-coupling coefficient Γ_j normalized to the self-coupling coefficient Γ_D in place of the power-domain α terms. The resulting coefficients and pressure-domain SPI values are reported in Table 5, alongside the power-domain SPI of Section 3 for comparison, consistent with the ~1 kPa shift of Figure 5.

Blower (header position)	Γ_j	**Pressure SPI**	**Power SPI**	**Interpretation**
D (0, target)	0.0631	100%	100%	Reference
C (1, adjacent)	0.0314	49.76%	2.92%	Pressure reveals Blower C's true coupling (17× the power SPI)
B (2, near)	0.0545	88.04%	9.10%	Pressure SPI 10× power SPI
A (3, far)	0.0474	75.11%	7.71%	Non-monotonic ordering confirmed independently

Table 5. Pressure-domain and power-domain SPI by blower and header position.

Whether the two configurations differ in steady-state pressure coupling is tested directly by pairing operating points with identical setpoints across ACD and BCD and comparing the operating-point-mean pressures. Across the 13 matched pairs, the mean pressure difference between configurations is −0.063 kPa, with a 95% confidence interval from −0.193 to +0.068 kPa. A paired t-test on 12 degrees of freedom returns $t = -1.05$ at p = 0.32, and Cohen's d of −0.29 indicates a small effect size. The interval includes zero and bounds any difference below approximately 0.5% of the mean manifold pressure, so at identical operating conditions the two configurations produce the same steady-state manifold pressure. This matched-condition null isolates any configuration difference to the fluctuation domain, which Section 5.3 quantifies.

The pressure regression resolves the non-monotonic puzzle of Section 3. In the power domain, Blower C's coupling appeared weak, because its flow-recession and head-loading terms partially cancel at Blower D's power. In the pressure domain, where no such cancellation occurs, Blower C's coupling is correctly revealed as strong, about seventeen times its power-domain value. The pressure SPI therefore measures the true coupling strength and confirms that all three neighbor blowers couple substantially to the manifold (50–88%), with the ordering C < A < B by header proximity to the manifold reference.

5.3 Coupling Energy Index

The Coupling Energy Index (CEI) quantifies how much of the manifold-pressure fluctuation energy is genuinely driven by the neighbor blower. The analysis band spans periods from 30 s to 512 s. The lower bound lies well above the 2 s Nyquist period of the 1 Hz acquisition, so the band is resolved without aliasing; the upper bound (512 s) is set by the Welch segment length and is contained within every operating-point record.

The CEI of operating point m is the coherence-weighted integral of the pressure power spectral density over the analysis band, i.e., the band-integrated coherent output power spectrum (Bendat and Piersol 2010),

$$CEI_m = \int_{1/512}^{1/30} \gamma_m^2(f) S_{\Delta p_m'}(f) df \quad [\mathrm{kPa}^2] \quad (5.2)$$

where $\gamma_m^2(f)$ is the magnitude-squared coherence between the neighbor blower's setpoint (the excitation) and the manifold pressure, $S_{\Delta p_m'}(f)$ is the one-sided power spectral density of $\Delta p_m'(t)$ (kPa²/Hz), and [1/512, 1/30] Hz is the analysis band, i.e. periods from 30 s to 512 s.

The CEI is not a new spectral quantity; it adapts the coherent output power (COP) spectrum, a coherence-based source-contribution technique formalized in the single-input/single-output spectral scheme of Bendat and Piersol [34]. For a linear system with a measured input and output, the ordinary coherence $\gamma^2(f)$ gives the fraction of the output auto spectrum that is linearly attributable to that input. The product $\gamma^2(f) \cdot S(f)$ is therefore the part of the output power explained by the input, while the remainder $[1 - \gamma^2(f)] \cdot S(f)$ arises from unmeasured inputs, nonlinearity, and noise [34], [35]. COP remains a standard tool for separating the contribution of a reference source from that of other incoherent sources measured at the same receiver. Recent work uses it to estimate the contribution of in-duct core-noise sources in aircraft engines from duct pressure sensors [36] and extends it to multiple partially coherent references with a significance threshold that suppresses spurious coherence arising from finite record lengths [35]. Here the same decomposition is carried over to the aerodynamic domain: the neighbor blower's setpoint acts as the reference source, the manifold pressure is the output, and integrating the COP over the analysis band yields a single energy attributable to inter-unit coupling. This complements earlier uses of pressure spectra to characterize blower flow phenomena [31], which describe the total fluctuation energy but do not attribute it to a specific source.

Inter-unit coupling and operational drift overlap in frequency and therefore cannot be separated by a frequency cut. The coherence weighting performs that separation instead: at each frequency it retains the fraction of the pressure fluctuation driven by the neighbor blower and suppresses the incoherent contributions of drift and measurement noise. The pressure spectral density is estimated by Welch's method (Welch 1967; Bendat and Piersol 2010), which splits the series into overlapping windowed segments and averages their periodograms to reduce the variance of the spectral estimate (Hann window, linear detrending). Applied to the 1 Hz pressure fluctuation series, this yields 7–9 independent frequency bins per operating point. Because Parseval's theorem states that a signal's total energy is the same in the time and frequency domains (Bendat and Piersol 2010), integrating the spectral density over frequency recovers the total fluctuation variance.

Figure 6a shows the resulting raw spectral density for a representative session (ACD, session 4); its energy is spread across the whole analysis band, with no isolated peak that would separate coupling from drift. The coherent fraction of the band energy is reported as, $Fraction_m =$

$100 \times CEI_m/E_{band,m}$ [%], where $E_{band,m}$ is the unweighted band energy of $\Delta p'_m(t)$, so the fraction gives the proportion of band fluctuation energy attributable to the neighbor blower.

The coherence between the neighbor blower's setpoint and the manifold pressure is shown in Figure 6b. It is substantial and broadband in every session, with session means of 0.51–0.90, so the coupling is coherent across the full analysis band rather than concentrated at any single frequency. Across the four stepping sessions the coherent fraction averages approximately 70% of the band fluctuation energy, with a range of 48–84% and a mean coherence of $\gamma^2 = 0.71$. Therefore, most of the manifold-pressure fluctuation is genuine inter-unit coupling rather than drift or noise.

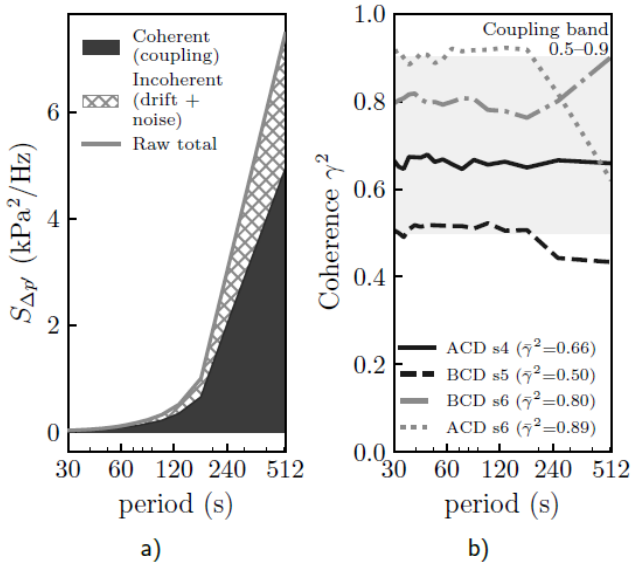


Figure 6. (a) Raw pressure spectral density for a representative session (ACD, session 4). (b) Magnitude-squared coherence γ² (period) between the neighbor blower's setpoint and the manifold pressure for all four stepping sessions.

The coherent CEI varies between repeated sessions of the same configuration by up to a factor of about 1.7 (ACD: 1.28 and 0.74 × 10^{-2} kPa²; BCD: 0.70 and 1.17 × 10^{-2} kPa²). This is an improvement over the raw fluctuation energy, whose session-to-session variability is larger, but the coupling energy retains appreciable session dependence, consistent with the day-to-day variation in the operating environment noted for the reproducibility of the within-session comparisons. On average, however, the two configurations are essentially equivalent in coupling energy (ACD/BCD ratio 1.08).

5.4 Cross-Validation Tests

Three tests cross-check the head-loading interpretation against the operating-point means (14 ACD operating points from session 4; 12 pooled BCD points): Test 1, the Pearson correlation between manifold pressure and Blower D power; Test 2, their partial correlation after residualizing both on Blower D's flow by ordinary least squares; and Test 3, a two-sided Mann–Whitney U comparison between configurations of the dimensionless ratio $\Pi_{op} = \Delta p \cdot Q_D / P_D$. Operating-point means use the recorded burst samples only; full results are given in Online Resource 4.

Pressure and Blower D power are positively correlated in both configurations, significantly for ACD ($r = 0.67$, $p = 0.009$) and marginally for BCD ($r = 0.53$, $p = 0.078$); apart from noise, the unexplained 55–72% of the pressure variance reflects the independent contribution of the neighbor blowers, which is the coupling signal. Controlling for Blower D's own flow largely removes the relationship: the partial correlation falls to $r = -0.04$ ($p = 0.89$) for BCD and to a non-significant $r = 0.44$ ($p = 0.11$, 11 residual degrees of freedom) for ACD, where part of the residual may stem from operating-point variation in the centerline-flow bias. The ratio Π_{op} is consistent across operating points (CV = 5.9% for ACD and 10.1% for BCD, the latter includes pooled session-to-session variation) and does not differ between configurations ($U = 87$, $p = 0.90$), both operating Blower D at $\Pi_{op} \approx 2.2$.

Π_{op} exceeds unity because Δp is the shared manifold pressure maintained by all three active blowers rather than Blower D's own head, and because the uncorrected centerline flow is high by 17–22%. What matters physically is its low within-configuration scatter and the absence of a between-configuration difference: Blower D operates at the same aerodynamic point whether the third active blower is A or B.

The three tests converge on a single picture: pressure and Blower D power are genuinely related, but the relationship is largely mediated by Blower D's flow, which is the head-loading signature in the operating-point-mean domain, and both configurations operate Blower D at the same aerodynamic ratio. Together with the matched-condition pressure null of Section 5.2, the directional flow signature of Section 4, the platykurtic distributions, and the sub-critical Greitzer B, these tests form a mutually consistent body of evidence for quasi-static head-loading coupling.

6. Energy Implications of Aerodynamic Coupling

6.1 Within-Operating-Point Fluctuation Penalty

The first mechanism is the additional power consumed at Blower D because of the continuous manifold pressure oscillations within an operating point. Because Blower D operates on a non-linear pressure-flow characteristic, fluctuating pressure produces a first-order power fluctuation proportional to the covariance of the pressure and flow fluctuations:

$$\delta P_{fluct} = \frac{\langle \Delta p_D'(t) \cdot Q_D'(t) \rangle}{\eta_f} \quad \text{[kW]} \quad (6.1)$$

where $\Delta p_D'(t)$and $Q_D'(t)$ are the zero-mean within-operating-point fluctuations of the manifold pressure and Blower D's flow, and the angle brackets denote a time average. An upper bound independent of the phase relationship follows from the Cauchy–Schwarz inequality: $\delta P_{fluct} \leq r_{PQ} \cdot \sigma_{\Delta p'} \cdot \frac{\sigma_{Q'}}{\eta_f}$. Where $r_{PQ} \leq 1$ is the correlation coefficient between the pressure and flow fluctuations. Because the Cauchy–Schwarz inequality guarantees that its magnitude cannot exceed unity, the bound is independent of the pressure–flow correlation and is evaluated at its limiting value of one, so that it reduces to the product of the two fluctuation standard deviations divided by the blower efficiency. Here $\sigma_{\Delta p'}$ is the within-operating-point pressure fluctuation standard deviation (σ_{noise}= 0.052 kPa, Section 5.1), $\sigma_{Q'}$ is the within-operating-point flow fluctuation standard deviation (≈ 0.0115 m^3/s $\approx 0.8\%$ of mean flow), and η_f is Blower D's overall efficiency, as in Section 3.3 ($\approx$ 0.70 for a turbo blower). Substituting these values gives an upper bound of $\approx$ 0.00085 kW (0.85 W), which relative to Blower D's mean operating power of approximately 25 kW is $\approx 0.0034\%$. Because the noise floor from Section 5.1 is estimated from the quietest settled operating points, it is a reference scale rather than the largest within-operating-point pressure fluctuation; however, the bound scales linearly with the pressure standard deviation, so even a fluctuation ten times larger ($\approx$0.5 kPa) would raise the penalty only to $\approx$8.5 W ($\approx$ 0.034% of Blower D's operating power), which remains negligible.

The fluctuation penalty is about four and a half orders of magnitude below Blower D's operating power and well below the resolution of the power analyzer. It is therefore negligible, physically unmeasurable, and excluded from the energy balance.

6.2 Transient Coupling Energy

The second mechanism is the transient excess power expended at Blower D during a neighbor-blower step change. It is the largest of the three but remains small in absolute terms. Consistent with the head-loading mechanism established in Section 3.3, an upward neighbor-blower step causes a Blower D power excursion that decays over the settling time. The energy of one such transient is the time integral of excess power.

If the transient is bounded by its peak deviation held over the settling time (a rectangular, conservative upper-bound approximation), the per-event energy is,

$$E_{trans,k} = \delta P_{D,k} \times \frac{t_{settle}}{60} \text{ [kWh]} \quad (6.2)$$

where $\delta P_{D,k}$ represents the peak power deviation at Blower D following step k (kW), from the NDTR extraction, t_{settle} is the settling time, the interval for the power to return within 5% of baseline. The base case considered is 1.0 min. Also, the expression is divided by 60 to convert from kW·min to kWh.

The peak deviation relates to the NDTR coupling gain of Section 4 by, $\delta P_{D,k} = \eta_k \cdot P_{pre.k} \cdot \frac{|\Delta u_{j,k}|}{u_{nom}}$, so that a known NDTR, η_k pre-step power, $P_{pre,k}$ and step magnitude fully determine the transient energy. Equation (6.2) adopts a rectangular (conservative upper-bound) profile; a triangular or exponential decay would reduce the energy by approximately a factor of two, and this is carried as the lower bound in the uncertainty analysis of Section 2.3.

Each per-step energy was computed from the extracted peak deviations via Eq. (6.2) and summed by configuration. Blower C upward steps dominate both configurations, contributing 84.9% of the ACD and 88.6% of the BCD transient energy, giving per-session totals of ≈0.028 kWh (ACD) and ≈0.012 kWh (BCD).

Both configurations therefore expend only a small transient coupling energy per equivalent session, ≈0.028 kWh (ACD) and ≈0.012 kWh (BCD), and this remains small across the plausible settling-time range. Because t_{settle} enters Eq. (6.2) as a linear multiplier, both totals scale proportionally and the configuration ratio (≈2.3×) is invariant, but it compares two small quantities. To annualize, the representative per-step energy of a single Blower C upward step (≈

0.0106 kWh) is scaled by the Blower C step rate; at the experimental rate of approximately 1.2 steps per hour this gives $\approx$111 kWh/yr. Set against the total system energy of approximately 657,000 kWh/yr (three blowers at $\approx$ 25 kW running continuously), this is $\approx$0.017% of system energy. Equating the annualized coupling energy to a 1% share of system consumption gives a break-even rate of approximately 70 setpoint changes per hour, one change roughly every 50 seconds, which is operationally unreachable.

6.3 Steady-State Energy Difference

The third mechanism asks whether the two configurations differ in sustained steady-state power at identical operating conditions. The matched-condition power difference $\Delta\bar{\mathcal{P}}_{D,l}$ for matched pair l (l = 1, …, N), where each pair consists of one ACD and one BCD operating point at the same operating condition and the overbar denotes the operating-point-mean power of Blower D, is:

$$\Delta\bar{\mathcal{P}}_{D,l} = \bar{P}_{D,\mathrm{ACD},l} - \bar{P}_{D,\mathrm{BCD},l} \quad [\mathrm{kW}] \quad (6.3)$$

A Wilcoxon signed-rank test on the $N = 11$ matched pairs returns no significant difference in median matched-condition power $\Delta\bar{\mathcal{P}}_{D,l}$, consistent with the head-loading mechanism established in Section 3.3. The test is underpowered: at the observed effect size (Cohen's $d \approx 0.09$) its power is only around 5.8%, and approximately 988 matched pairs would be required for 80% power, so a small true difference cannot be excluded.

Because the matched-condition power difference is statistically null (Eq. (6.3); Wilcoxon signed-rank test, not significant), the steady-state energy difference between configurations is likewise null. As a separate, corroborating result, the matched-condition pressure comparison of Section 5.2 also shows no significant difference between configurations, and the cross-validation tests of Section 5.4 confirm that the two configurations operate the instrumented blower at the same aerodynamic ratio. The steady state contribution to coupling energy is therefore negligible, consistent with the small transient and fluctuation contributions.

The coupling identified in Sections 4 and 5 is therefore real and directionally identifiable, but energetically small relative to system consumption under any realistic setpoint-change rate. The contribution of this work is the identification and physical mechanism of coupling rather than energy saving.

7. Conclusions

This work characterized the aerodynamic coupling between blowers discharging into a shared manifold, identifying its mechanism from the steady-state operating point through the transient response to the manifold pressure field. Five findings follow.

The coupling is real and reproducible. The identified coupling coefficients reproduced across two independent sessions recorded on different days, with the self-coupling coefficient agreeing to within 0.02%, confirming a stable physical relationship rather than a session-specific artifact.

The power-domain coupling is non-monotonic in distance. The adjacent Blower C couples most weakly (power SPI 2.9%), while the more distant Blowers A and B couple more strongly (7.7% and 9.1%). This counter-intuitive ordering is resolved in the pressure domain, where Blower C's coupling (SPI 49.8%) is about seventeen times its power-domain value; proximity therefore does not predict coupling strength in the power domain.

The coupling is a flow-domain phenomenon with a directional signature. The power response is uniformly small and does not distinguish the blowers. The coupling is instead carried by the flow channel, whose sign reverses with step direction (negative on upward steps, positive on downward; sign test $p = 0.001$). This sign reversal is the signature of genuine manifold head-loading, distinguishing it from simple flow superposition, and it is resolved only because power and flow were measured simultaneously.

The manifold operates in a quasi-static regime, and the configurations are equivalent at steady state. All operating points are platykurtic and the Greitzer parameter (B = 0.23–0.32) lies far below surge; multiple independent tests confirm the two configurations are equivalent in steady-state coupling (ACD/BCD ratio 1.08), with only residual session-to-session variability.

The coupling's significance is dynamical rather than energetic: all three energy mechanisms (fluctuation, transient, and steady state) remain below 0.02% of annual system consumption, and neither configuration holds an energy advantage.

Future work should test whether the non-monotonic, position-dependent coupling generalizes to larger and more heterogeneous manifolds; develop a supervisory strategy that minimizes high-coupling step events in place of equal-speed or fixed-staging heuristics; and

embed the identified steady-state and transient models into a predictive, plant-deployable controller.

Authorship contributions

Paulo Cesar Correa Galeano was responsible for writing – review &editing, writing – original draft, visualization, validation, methodology, investigation, formal analysis, data curation, conceptualization. Yu-Jeng Lin took care of visualization and data curation. Chen-yang Lan was involved in writing – review & editing, supervision, project administration, methodology, funding acquisition, conceptualization.

Acknowledgements

This work was supported by the National Science and Technology Council (NSTC) of Taiwan under Grant No. NSTC 115-2221-E-011-178. The support provided by the Taiwan Tech SEV Research Center at National Taiwan University of Science and Technology, which is funded as a Featured Areas Research Center by the Ministry of Education, Taiwan, R.O.C., and the Industry-University Cooperation Project with Innolux Corporation is gratefully acknowledged. This is a collaborative research between UPTP and NTUST.

Data availability

The data that support the findings of this study are available from the corresponding author upon reasonable request.

References

Arya RK (2025) Compressors and Blowers: Maintenance, Practical Guidance, Energy-Efficient Technologies, 1st ed. Walter de Gruyter GmbH, Berlin/Boston

Bendat JS, Piersol AG (2010) Random data: analysis and measurement procedures, 4th ed. Wiley, Hoboken, N.J

978 Bristol E (1966) On a new measure of interaction for multivariable process control. IEEE Trans
979 Autom Control 11:133–134. https://doi.org/10.1109/TAC.1966.1098266

980 Chatterjee A, Zhang L, Xia X (2015) Optimization of mine ventilation fan speeds according to
981 ventilation on demand and time of use tariff. Appl Energy 146:65–73.
982 https://doi.org/10.1016/j.apenergy.2015.01.134

983 Conrad D, Mayer J, Reichert E (2023) Optimization, Control, and Design of Arbitrarily Shaped
984 Fan Arrays. Int J Turbomach Propuls Power 8:12. https://doi.org/10.3390/ijtpp8020012

985 Czyżewicz J, Jaskólski P, Ziemiański P, et al (2022) Towards Designing an Innovative Industrial
986 Fan: Developing Regression and Neural Models Based on Remote Mass Measurements.
987 Energies 15:2425. https://doi.org/10.3390/en15072425

988 De Souza E (2015) Improving the energy efficiency of mine fan assemblages. Appl Therm Eng
989 90:1092–1097. https://doi.org/10.1016/j.applthermaleng.2015.04.048

990 Dong H, Jiang J (2025) Experimental study on serial and parallel operation of fans based on
991 flexible duct. J Phys Conf Ser 2932:012034. https://doi.org/10.1088/1742-
992 6596/2932/1/012034

993 Fulpagare Y, Chiou J-H, Liao Y-H, Wang C-C (2025) Optimized and energy efficient server fan
994 control using deep reinforcement learning method. J Build Eng 104:112306.
995 https://doi.org/10.1016/j.jobe.2025.112306

996 Fulpagare Y, Huang K-R, Liao Y-H, Wang C-C (2022) Optimal energy management for air
997 cooled server fans using Deep Reinforcement Learning control method. Energy Build
998 277:112542. https://doi.org/10.1016/j.enbuild.2022.112542

999 Greitzer EM (1976) Surge and Rotating Stall in Axial Flow Compressors—Part I: Theoretical
1000 Compression System Model. J Eng Power 98:190–198.
1001 https://doi.org/10.1115/1.3446138

1002 Gunner A, Afshari A, Bergsøe NC, et al (2016) Energy savings and manifold supply ventilation
1003 systems. J Build Eng 7:71–77. https://doi.org/10.1016/j.jobe.2016.04.004

1004 Harris CR, Millman KJ, Van Der Walt SJ, et al (2020) Array programming with NumPy. Nature
1005 585:357–362. https://doi.org/10.1038/s41586-020-2649-2

1006 International Organization for Standardization (ISO) (2017) Fans — Performance testing using
1007 standardized airways

1008 Jia W, Liu T, Kong Q, et al (2025) Aero-propulsive interaction analysis of a distributed
1009 propulsion system under windmilling conditions. Phys Fluids 37:067110.
1010 https://doi.org/10.1063/5.0271760

Liśkiewicz G, Horodko L, Stickland M, Kryłowicz W (2014) Identification of phenomena preceding blower surge by means of pressure spectral maps. Exp Therm Fluid Sci 54:267–278. https://doi.org/10.1016/j.expthermflusci.2014.01.002

Ljung L (1999) System identification: theory for the user, 2nd ed. Prentice Hall PTR, Upper Saddle River, NJ

Ostmann P, Kremer MT, Mathis P, Müller D (2022) Efficiency Increase of Air Handling Units by Parallely Operated Fans. Vent 2022 13th Int Ind Vent Conf Contam Control 2022-06-22-2022-06–24:pages 298-306. https://doi.org/10.18154/RWTH-2022-08049

Ostmann P, Rätz M, Kremer M, Müller D (2024) Prediction of Fan Array Performance with Polynomial and Support Vector Regression Models. Int J Turbomach Propuls Power 9:32. https://doi.org/10.3390/ijtpp9040032

Perry AT, Ansell PJ, Kerho MF (2018) Aero-Propulsive and Propulsor Cross-Coupling Effects on a Distributed Propulsion System. J Aircr 55:2414–2426. https://doi.org/10.2514/1.C034861

Rao P, Sheaffer P, Chen Y, et al (2021) U.S. Industrial and Commercial Motor System Market Assessment Report Volume 1: Characteristics of the Installed Base

Schlichting (Deceased) H, Gersten K (2017) Boundary-Layer Theory, 9th ed. 2017. Springer, Berlin, Heidelberg

Seabold S, Perktold J (2010) Statsmodels: Econometric and Statistical Modeling with Python. Austin, Texas, pp 92–96

Shi S, Miyata S, Akashi Y, et al (2024) Model-based optimal control strategy for multizone VAV air-conditioning systems for neutralizing room pressure and minimizing fan energy consumption. Build Environ 256:111464. https://doi.org/10.1016/j.buildenv.2024.111464

Shim G, Song L, Wang G (2014) Comparison of different fan control strategies on a variable air volume systems through simulations and experiments. Build Environ 72:212–222. https://doi.org/10.1016/j.buildenv.2013.11.003

Siddiqui MAH, Raj P, Ansari S, et al (2025) Maximizing energy savings in coal mines industrial ventilation: strategies and analysis for power reduction. Discov Appl Sci 7:423. https://doi.org/10.1007/s42452-025-06989-0

Su Y, Chen X, Liu X, et al (2023) Study of Parallel Compressor System and Real-Time Simulation Based on Modular Dynamic System Greitzer Modeling. Machines 11:. https://doi.org/10.3390/machines11020213

Virtanen P, Gommers R, Oliphant TE, et al (2020) SciPy 1.0: fundamental algorithms for scientific computing in Python. Nat Methods 17:261–272. https://doi.org/10.1038/s41592-019-0686-2

Weinstein R, Spada VA, Simmons BM (2026) Experimental Study of Aeropropulsive Interactions for Electric Ducted Fans on a Wing. J Aircr 1–23. https://doi.org/10.2514/1.C038401

Welch P (1967) The use of fast Fourier transform for the estimation of power spectra: A method based on time averaging over short, modified periodograms. IEEE Trans Audio Electroacoustics 15:70–73. https://doi.org/10.1109/TAU.1967.1161901